actuators

MDPI

Article

Design of a Suspension Controller with an Adaptive Feedforward Algorithm for Ride Comfort Enhancement and Motion Sickness Mitigation

Jinwoo Kim and Seongjin Yim *

Department of Mechanical and Automotive Engineering, Seoul National University of Science and Technology, 232 Gongneung-ro, Nowon-gu, Seoul 01811, Republic of Korea; king@g.seoultech.ac.kr
* Correspondence: acebtif@seoultech.ac.kr; Tel.: +82-2-970-9011

Abstract: This paper presents a design method of a suspension controller with an adaptive feedforward algorithm for ride comfort enhancement and motion sickness mitigation. Recently, it was shown that motion sickness is caused by combined heave and pitch motions of a sprung mass within the range of 0.8 and 8 Hz. For this reason, it is necessary to design a suspension controller for the purpose of reducing the heave and pitch vibration of a sprung mass within this range. To represent the heave acceleration and the pitch rate of a sprung mass, a 4-DOF half-car model is adopted as a vehicle model. For easy implementation in a real vehicle, a static output feedback control is adopted instead of a full-state one. To reduce the heave acceleration of a sprung mass for ride comfort enhancement, a linear quadratic SOF controller is designed. To reduce the pitch rate of a sprung mass for motion sickness mitigation, a filtered-X LMS algorithm is applied. To validate the method, simulation on vehicle simulation software is conducted. From the simulation results, it is shown that the proposed method is effective for ride comfort enhancement and motion sickness mitigation.

Keywords: motion sickness; static output feedback control; adaptive feedforward algorithm; filtered-X LMS algorithm; half-car model; heave acceleration; pitch rate

check for updates

Citation: Kim, J.; Yim, S. Design of a Suspension Controller with an Adaptive Feedforward Algorithm for Ride Comfort Enhancement and Motion Sickness Mitigation. *Actuators* **2024**, *13*, 315. https://doi.org/10.3390/act13080315

Academic Editor: Takeshi Mizuno

Received: 22 July 2024
Revised: 13 August 2024
Accepted: 19 August 2024
Published: 20 August 2024

Copyright: © 2024 by the authors. Licensee MDPI, Basel, Switzerland. This article is an open access article distributed under the terms and conditions of the Creative Commons Attribution (CC BY) license (https://creativecommons.org/licenses/by/4.0/).

1. Introduction

Since the late 2000s, autonomous driving has been extensively studied in a wide range of the engineering field [1–3]. Autonomous driving has been expected to provide several benefits such as the conversion from an active driver to a passive passenger, transition from driving tasks to non-driving ones, and rearward facing seating arrangements [4–6]. However, those scenarios may lead to a visual–vestibular conflict, which has been known as a main cause of motion sickness [4,5]. In other words, these benefits to a driver can cause motion sickness more easily and severely. For this reason, it is necessary to prepare the mitigation of motion sickness when designing autonomous driving functions.

Figure 1 shows the frequency weighting curves specified in ISO2631-1, which are used to evaluate the relationships between vibration frequency and human responses [7,8]. In Figure 1, the weight $\mathbf{W_k}$:**V** represents the heave acceleration (a_z) related to ride comfort over the frequency range from 4.0 to 10.0 Hz, and the weight $\mathbf{W_k}$:**H** reflects the fact that human bodies are most sensitive to the frequency range of 0.5 to 2.0 Hz in the horizontal direction. For ride comfort enhancement, this range of a_z should be reduced by a suspension control method [7]. The weight $\mathbf{W_f}$:**MS** represents vertical vibration over the frequency range from 0.1 to 0.2 Hz, and is related to motion sickness. For motion sickness mitigation, this range of a_z should be reduced. As shown in Figure 1, the weight $\mathbf{W_f}$:**MS** is separated from $\mathbf{W_k}$:**V**. However, ISO2631-1 originated from vibration data measured on a ship [7]. In other words, it has not reflected the characteristics of motion sickness of a car.

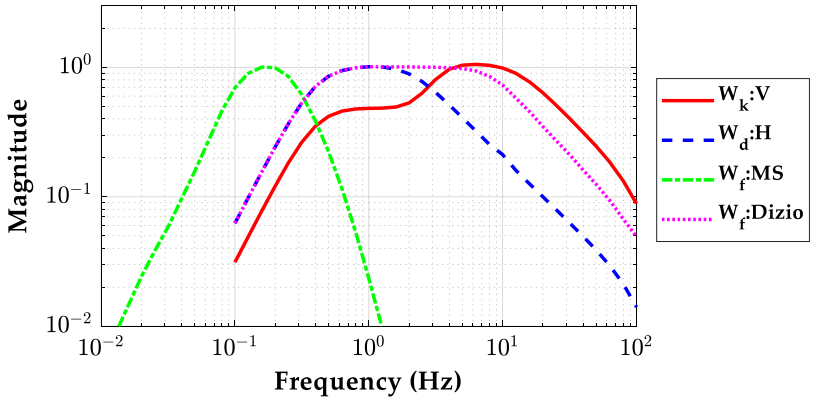


Figure 1. Frequency weighting curves given in ISO 2631-1 [7,9] and presented by Dizio [10,11].

Since the mid-2010s, it has been reported that motion sickness is made worse by the combination of a_z and the pitch rate (ω_y) of a sprung mass (SPM) in the frequency range of 0.8 to 8.0 Hz, shown as $\mathbf{W_f}$:**Dizio** in Figure 1 [10,11]. Different from $\mathbf{W}_k$:**V** and $\mathbf{W_f}$:**MS**, $\mathbf{W_f}$:**Dizio** overlaps with $\mathbf{W_k}$:**V** in the frequency range of 4.0 to 10.0 Hz. For this reason, ride comfort can be improved and motion sickness can be mitigated if a controller reduces the a_z and ω_y of an SPM in the frequency range of 0.8 to 8.0 Hz. Based on this fact, the goal of this paper to design a suspension controller for ride comfort enhancement and motion sickness mitigation. For this purpose, the previous works adopted a static output feedback (SOF) control method and applied it to reduce the a_z and ω_y of an SPM with active suspension [9,12].

For the last five decades, various control methods with an actuator in the suspension have been proposed and applied to suspension control in order to enhance ride comfort and road holding [13–15]. For suspension control, several actuators such as active, semi-active and pneumatic actuators have been used [13]. In this paper, among them, an active suspension is selected as an actuator, which can generate vertical force in the suspension [9,12].

To date, various controller design methodologies have been applied for active suspension control [16–19]. Among controller design methodologies, a linear quadratic regulator (LQR) is the most widely adopted controller for active suspension control, in view of the fact that it is easy to tune finely in terms of a particular objective [20]. An LQR is designed with a state-space equation (SSE) and an LQ cost function. To represent the a_z and ω_y of an SPM, a half-car model is selected. From a half-car model with a linear spring and damper, a linear SSE is derived.

The structure of the LQR is one of full-state feedback, which requires all system states to be measured. However, it is hard to measure or estimate all system states in real vehicles. Moreover, the number of elements in the gain matrix of an LQR is large, which makes it harder to implement on real vehicles. To deal with the problem, an SOF control has been adopted because it uses only sensor outputs which are available in real vehicles [9,12,21,22]. Specifically, the previous works have used only two and three sensor outputs for the half-car and full-car models, respectively [23,24]. Accordingly, SOF is selected as a control structure in this paper.

In this paper, the SOF controller uses heave velocities at the front/rear corners of an SPM as an available sensor output for feedback. The half-car model has two control inputs. Consequently, the SOF controller has a gain matrix with 2×2 dimensions. Moreover, two SOF controllers with two gain elements are proposed by using the symmetry between the front/rear corners with the pitch motion of an SPM [12]. These SOF controllers are easier to implement in real vehicles because they have two gain elements and require two sensor signals for feedback [12]. Moreover, for the same reason, it is also easier and simpler to optimize these SOF controllers with an LQ cost function. To optimize the gain matrices of SOF controllers, a heuristic optimization method, CMA-ES, is applied in this paper [25,26].

For the last four decades, preview control has been studied and applied for suspension control [20]. Among several schemes in the area of preview control, a wheelbase preview control scheme (WBPCS) has been known to be effective for suspension control and easy to implement in real vehicles. Figure 2 shows a diagram of a WBPCS. As shown in Figure 2, a WBPCS uses a signal measured at the front suspension or front corners of an SPM and controls an actuator at the rear suspension. A controller in a WBPCS is inherently a feedforward one because it uses a signal obtained from the front suspension. For example, in LQ optimal preview control, a WBPCS estimates a road profile with an observer and measured signals at the front suspension, and generates a control input from a LQ optimal controller at the rear suspension [20]. In this paper, a WBPCS is adopted for the purpose of reducing the ω_y of an SPM for motion sickness mitigation.

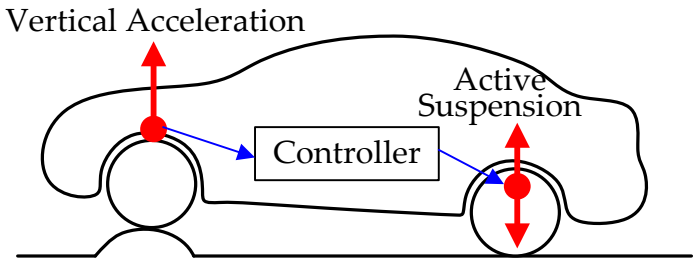


Figure 2. Schematic diagram of wheelbase preview control.

In WBPCS, a filtered-X LMS (FxLMS) algorithm has been adopted as a feedforward adaptive controller [27,28]. To date, FxLMS has been applied to active noise control (ANC) [29,30]. Moreover, it has also been applied to vibration suppression and vehicle suspension control [31–41]. As shown in Figure 2, the vertical acceleration measured at the front corner of the SPM is selected as a reference signal of FxLMS. This signal is relatively easy to measure with an accelerometer. The actuator is an active suspension located on the rear suspension [31].

To validate the performance of the SOF controllers and FxLMS algorithm, simulation is carried out on vehicle simulation software. Based on simulation results, the effect of FxLMS combined with SOF controllers is shown, in terms of ride comfort and motion sickness.

The goal of this paper is to design SOF controllers and an FxLMS algorithm for ride comfort enhancement and motion sickness mitigation. The contributions of this paper can be summarized as follows:

1. SOF controllers are designed to reduce the a_z and ω_y of an SPM over the frequency range of 0.8 to 8.0 Hz. Using the vertical velocities at the front/rear corners of an SPM and SSE from a half-car model, three SOF controllers are proposed.
2. To reduce the ω_y of an SPM over the frequency range of 0.8 to 8.0 Hz, an FxLMS algorithm is applied to the framework of a WBPCS.
3. With SOF controllers and an FxLMS algorithm, simulation is conducted on CarSim. From simulation results, it is observed which SOF controller is better for ride comfort enhancement and whether FxLMS is effective or not for motion sickness mitigation.

This paper is made up of five sections. A half-car model is presented and its SSE is derived in Section 2. With the SSE, three SOF controllers are proposed and SOF controllers are designed with the optimal LQ control method. FxLMS is designed in Section 3. In Section 4, simulation with designed controllers is conducted on CarSim and simulation results are analyzed. The conclusions are given in Section 5.

2. Design of LQ SOF Controllers

In this section, the SSE is derived from a half-car model, as presented in previous studies [12]. With the SSE and LQ cost function defined for ride comfort enhancement and motion sickness mitigation, LQ SOF controllers are proposed and designed. As an adaptive feedforward controller, an FxLMS algorithm is applied for pitch rate control.

Figure 3 shows the controller structure for suspension control with the LQ SOF controller and FxLMS algorithm. In Figure 3, red and blue circles represent accelerometers and active suspensions at the front/rear corners, respectively. a_{zf} and a_{zr} are the vertical accelerations measured with those accelerometers. As shown in Figure 3, LQ SOF controllers use the vertical accelerations measured at the front/rear corners and send control commands to the front/rear active suspensions, and FxLMS uses the vertical acceleration measured at the front suspension and sends control commands to the rear active suspension.

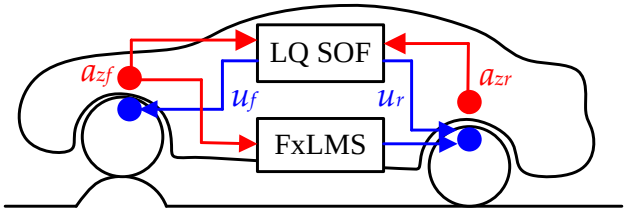


Figure 3. Controller structure for suspension control.

2.1. Half-Car Model and State-Space Equation

When designing optimal LQ controllers such as LQR and LQ SOF ones, an SSE is needed. Generally, an SSE is derived from a linear vehicle model. To describe the heave and pitch motions of an SPM, a half-car model is selected as a vehicle model in this paper [12]. Figure 4 shows the half-car model with linear springs and dampers. In Figure 4, S_f and S_r stand for the front/rear suspensions. u_f and u_r are the control input or the vertical control force generated by an active actuator in the front/rear suspensions. The parameters in the half-car model are described in the Nomenclature. Let us denote the front/rear corners of the SPM as the SPMFC and SPMRC, respectively. In Figure 4, z_{sf} and z_{sr} are the vertical displacements of the SPMFC and SPMRC, respectively. acm_f and acm_r are the accelerometers attached to the SPMFC and SPMRC, respectively.

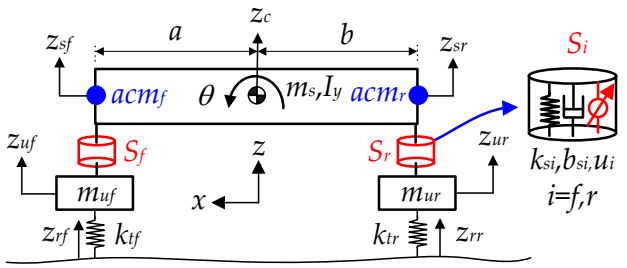


Figure 4. Half-car model with linear springs and dampers.

In Figure 4, the forces at the front/rear suspensions are derived as in (1). With (1) and the geometric relationship shown in Figure 4, the equations of motions of the sprung mass, m_s, and the unsprung masses, m_{uf} and m_{ur}, are derived as in (2). Using the geometric relationship and the approximation, $\sin\theta \approx \theta$, z_{sf} and z_{sr} are calculated as in (3) from z_c and θ of the SPM. Equation (3) is converted into (4). New vectors and a matrix are defined in Equation (5). In (5), the vectors of state variables, disturbances and control inputs, i.e., **x**, **w** and **u**, are defined, where those vectors have 8 states, 2 disturbances and 2 control inputs, respectively. With those definitions in (5), (4) is converted into Equation (6). Equation (6) represents the geometric relationship between the heave and pitch motions of the SPM and the vertical motions of the SPMFC and SPMRC.

$$\begin{cases} f_f = -k_{sf}(z_{si} - z_{ui}) - b_{sf}(\dot{z}_{si} - \dot{z}_{ui}) + u_f \\ f_r = -k_{sr}(z_{si} - z_{ui}) - b_{sr}(\dot{z}_{si} - \dot{z}_{ui}) + u_r \end{cases} \quad (1)$$

$$\begin{cases} m_s\ddot{z}_c = f_f + f_r \\ I_y\ddot{\theta} = -af_f + bf_f \end{cases} \quad \begin{cases} m_{uf}\ddot{z}_{uf} = -f_f - k_{tf}(z_{uf} - z_{rf}) \\ m_{ur}\ddot{z}_{ur} = -f_r - k_{tr}(z_{ur} - z_{rr}) \end{cases} \tag{2}$$

$$\begin{cases} z_{sf} = z_c - a\sin\theta \simeq z_c - a\theta \\ z_{sr} = z_c + b\sin\theta \simeq z_c + b\theta \end{cases} \tag{3}$$

$$\begin{bmatrix} z_{sf} \\ z_{sr} \end{bmatrix} = \begin{bmatrix} 1 & -a \\ 1 & b \end{bmatrix} \begin{bmatrix} z_c \\ \theta \end{bmatrix} \tag{4}$$

$$\begin{gathered} \mathbf{p} \equiv \begin{bmatrix} z_c \\ \theta \end{bmatrix},\ \mathbf{z}_s \equiv \begin{bmatrix} z_{sf} \\ z_{sr} \end{bmatrix},\ \mathbf{z}_u \equiv \begin{bmatrix} z_{uf} \\ z_{ur} \end{bmatrix},\ \mathbf{z} \equiv \begin{bmatrix} \mathbf{p} \\ \mathbf{z}_u \end{bmatrix},\ \mathbf{f} \equiv \begin{bmatrix} f_f \\ f_r \end{bmatrix},\ \mathbf{H} \equiv \begin{bmatrix} 1 & 1 \\ -a & b \end{bmatrix} \\ \mathbf{x} \equiv \begin{bmatrix} \mathbf{z} \\ \dot{\mathbf{z}} \end{bmatrix},\ \mathbf{w} = \mathbf{z}_r \equiv \begin{bmatrix} z_{rf} \\ z_{ru} \end{bmatrix},\ \mathbf{u} \equiv \begin{bmatrix} u_f \\ u_r \end{bmatrix} \\ \mathbf{M}_s \equiv \mathrm{diag}(m_s, I_y),\ \mathbf{M}_u \equiv \mathrm{diag}\left(m_{uf}, m_{ur}\right) \\ \mathbf{K}_s \equiv \mathrm{diag}\left(k_{sf}, k_{sr}\right),\ \mathbf{B}_s \equiv \mathrm{diag}\left(b_{sf}, b_{sr}\right),\ \mathbf{K}_t \equiv \mathrm{diag}\left(k_{tf}, k_{tr}\right) \end{gathered} \tag{5}$$

$$\mathbf{z}_s = \mathbf{H}^T\mathbf{p} \tag{6}$$

By using the vectors and matrices defined in (5) and replacing $\mathbf{z}_s$ with (6), (1) and (2) are converted into (7) and (8), respectively. By replacing $\mathbf{f}$ in (8) with (7), (9) is obtained. By rearranging (9), it is converted into (10) and becomes (11). With the definition of $\mathbf{x}$ in (5), (11) is converted into (12) and becomes the SSE, (13). A detailed derivation procedure of the SSE (13) can be found in previous research [9,12].

$$\begin{aligned} \mathbf{f} &= -\mathbf{K}_s(\mathbf{z}_s - \mathbf{z}_u) - \mathbf{B}_s(\dot{\mathbf{z}}_s - \dot{\mathbf{z}}_u) + \mathbf{u} \\ &= -\mathbf{K}_s(\mathbf{H}^T\mathbf{p} - \mathbf{z}_u) - \mathbf{B}_s(\mathbf{H}^T\dot{\mathbf{p}} - \dot{\mathbf{z}}_u) + \mathbf{u} \end{aligned} \tag{7}$$

$$\begin{cases} \mathbf{M}_s\ddot{\mathbf{p}} = \mathbf{H}\mathbf{f} \\ \mathbf{M}_u\ddot{\mathbf{z}}_u = -\mathbf{f} - \mathbf{K}_t(\mathbf{z}_u - \mathbf{z}_r) \end{cases} \tag{8}$$

$$\begin{cases} \mathbf{M}_s\ddot{\mathbf{p}} = -\mathbf{H}\mathbf{K}_s(\mathbf{H}^T\mathbf{p} - \mathbf{z}_u) - \mathbf{H}\mathbf{B}_s(\mathbf{H}^T\dot{\mathbf{p}} - \dot{\mathbf{z}}_u) + \mathbf{H}\mathbf{u} \\ \mathbf{M}_u\ddot{\mathbf{z}}_u = \mathbf{K}_s(\mathbf{H}^T\mathbf{p} - \mathbf{z}_u) + \mathbf{B}_s(\mathbf{H}^T\dot{\mathbf{p}} - \dot{\mathbf{z}}_u) - \mathbf{u} - \mathbf{K}_t(\mathbf{z}_u - \mathbf{z}_r) \end{cases} \tag{9}$$

$$\underbrace{\begin{bmatrix} \mathbf{M}_s & \mathbf{0}_{2\times2} \\ \mathbf{0}_{2\times2} & \mathbf{M}_u \end{bmatrix}}_{\mathbf{M}} \begin{bmatrix} \ddot{\mathbf{p}} \\ \ddot{\mathbf{z}}_u \end{bmatrix} = \underbrace{\begin{bmatrix} -\mathbf{H}\mathbf{K}_s\mathbf{H}^T & \mathbf{H}\mathbf{K}_s \\ \mathbf{K}_s\mathbf{H}^T & -\mathbf{K}_s - \mathbf{K}_t \end{bmatrix}}_{\mathbf{E}} \begin{bmatrix} \mathbf{p} \\ \mathbf{z}_u \end{bmatrix} + \underbrace{\begin{bmatrix} -\mathbf{H}\mathbf{B}_s\mathbf{H}^T & \mathbf{H}\mathbf{B}_s \\ \mathbf{B}_s\mathbf{H}^T & -\mathbf{B}_s \end{bmatrix}}_{\mathbf{F}} \begin{bmatrix} \dot{\mathbf{p}} \\ \dot{\mathbf{z}}_u \end{bmatrix} + \underbrace{\begin{bmatrix} \mathbf{0}_{2\times2} \\ \mathbf{K}_t \end{bmatrix}}_{\mathbf{G}} \mathbf{z}_r + \underbrace{\begin{bmatrix} \mathbf{H} \\ -\mathbf{I}_{2\times2} \end{bmatrix}}_{\mathbf{L}} \mathbf{u} \tag{10}$$

$$\mathbf{M}\ddot{\mathbf{z}} = \mathbf{E}\mathbf{z} + \mathbf{F}\dot{\mathbf{z}} + \mathbf{G}\mathbf{w} + \mathbf{L}\mathbf{u} \tag{11}$$

$$\begin{bmatrix} \dot{\mathbf{z}} \\ \ddot{\mathbf{z}} \end{bmatrix} = \underbrace{\begin{bmatrix} \mathbf{0}_{4\times4} & \mathbf{I}_{4\times4} \\ \mathbf{M}^{-1}\mathbf{E} & \mathbf{M}^{-1}\mathbf{F} \end{bmatrix}}_{\mathbf{A}} \begin{bmatrix} \mathbf{z} \\ \dot{\mathbf{z}} \end{bmatrix} + \underbrace{\begin{bmatrix} \mathbf{0}_{4\times2} \\ \mathbf{M}^{-1}\mathbf{G} \end{bmatrix}}_{\mathbf{B}_1} \mathbf{w} + \underbrace{\begin{bmatrix} \mathbf{0}_{4\times2} \\ \mathbf{M}^{-1}\mathbf{L} \end{bmatrix}}_{\mathbf{B}_2} \mathbf{u} \tag{12}$$

$$\dot{\mathbf{x}} = \mathbf{A}\mathbf{x} + \mathbf{B}_1\mathbf{w} + \mathbf{B}_2\mathbf{u} \tag{13}$$

2.2. Design of LQR

A LQ cost function for ride comfort enhancement and motion sickness mitigation is given as (14). In the LQ cost function, a particular objective can be obtained by setting the corresponding weight higher or lower while fixing the other weights as constant. In (14), the weight ρ_i in J is set with Bryson's rule, as given in (15), where ξ_i is the maximum allowable value (MAV) for the i-th term [42]. For ride comfort enhancement, ξ_1 for a_z should be set as small as possible. For motion sickness mitigation, ξ_1 for a_z and ξ_3 for ω_y should be set as small as possible. The new vector $\mathbf{v}$ and the matrices, $\mathbf{Q}$, $\mathbf{N}$ and $\mathbf{R}$, are defined in (16). With those vectors and matrices, the LQ cost function, (14), is converted

into (17). With the matrices **A**, $\mathbf{B}_2$, **Q**, **N** and **R** in (17), the LQR is obtained as the full-state feedback form of (18).

$$J = \int_0^\infty \left\{ \begin{array}{c} \rho_1 \ddot{z}_c^2 + \rho_2 \ddot{\theta}^2 + \rho_3 \dot{\theta}^2 + \rho_4 \theta^2 \\ +\rho_5 \sum\limits_{i=f,r} (z_{si} - z_{ui})^2 + \rho_6 \sum\limits_{i=f,r} (z_{ui} - z_{ri})^2 + \rho_7 \sum\limits_{i=f,r} u_i^2 \end{array} \right\} dt \tag{14}$$

$$\rho_i = \frac{1}{\xi_i^2},\ i = 1, 2, \cdots, 7 \tag{15}$$

$$\left\{ \begin{array}{l} \mathbf{v} \equiv \mathbf{W}\mathbf{x} + \mathbf{V}\mathbf{u} \\ \mathbf{Q} \equiv \mathbf{W}^T\mathbf{W},\ \mathbf{N} \equiv \mathbf{W}^T\mathbf{V},\ \mathbf{R} \equiv \mathbf{V}^T\mathbf{V} \end{array} \right. \tag{16}$$

$$J = \int_0^\infty \mathbf{v}^T \mathbf{v} dt = \int_0^\infty \left\{ \begin{bmatrix} \mathbf{x} \\ \mathbf{u} \end{bmatrix}^T \begin{bmatrix} \mathbf{Q} & \mathbf{N} \\ \mathbf{N}^T & \mathbf{R} \end{bmatrix} \begin{bmatrix} \mathbf{x} \\ \mathbf{u} \end{bmatrix} \right\} dt \tag{17}$$

$$\mathbf{u} = -\mathbf{K}_{LQR}\mathbf{x} = -\mathbf{R}^{-1}\mathbf{B}_2^T\mathbf{P}\mathbf{x} \tag{18}$$

2.3. Design of LQ SOF Controllers

Generally, it is not easy for one to measure all of the state variables of **x** in real vehicles due to the fact that there are no sensors to measure it or the fact that sensors are expensive. Moreover, full-state feedback has a lot of gain elements to be tuned. For those reasons, LQR is difficult to implement in real vehicles. To cope with those problems, a static output feedback (SOF) control has been selected as a controller structure. An SOF controller uses sensor signals available in real vehicles for feedback. The typical sensor used for suspension control is an accelerometer, which is installed on the SPMFC, SPMRC and wheel centers. In this paper, an SOF controller uses the vertical velocities at the SPMFC and SPMRC, which are calculated from the accelerometer signals.

Figure 5 shows the block diagram that represents the calculation procedure for the vertical velocities at the front/rear corners. To measure the vertical accelerations at the front/rear corners, acm_f and acm_r are installed on the SPMFC and SPMRC, as shown in Figure 4 [43–45]. These accelerometer signals are filtered sequentially through high-pass and low-pass filters to reject DC offset and sensor noise, respectively. These filters were given in the reference [9].

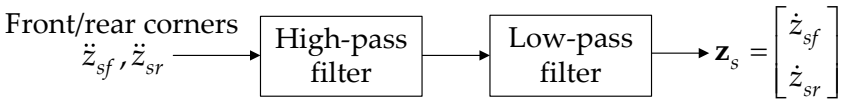


Figure 5. Block diagram for calculation of vertical velocities at front/rear corners.

The vector of two available sensor outputs, **y**, is defined from the state vector **x** as in (19). With those outputs, three SOF controllers, $\mathbf{u}_{SOF}$, $\mathbf{u}_{SSOF1}$ and $\mathbf{u}_{SSOF2}$, are proposed as in (20) [9]. For $\mathbf{u}_{SSOF1}$ and $\mathbf{u}_{SSOF2}$ in (20), the subscript *SSOF* means a structured SOF, where only two gains are used in the controller gain matrices, $\mathbf{K}_{SSOF1}$ and $\mathbf{K}_{SSOF2}$. The structured SOF controller, $\mathbf{K}_{SSOF1}$, reflects the symmetry between SPMFC and SPMRC along the pitch motion of the SPM. On the other hand, the vertical motions of the SPMFC and SPMRC are independent of each other in the structured SOF controller, $\mathbf{K}_{SSOF2}$.

$$\mathbf{y} = \begin{bmatrix} \dot{z}_{sf} \\ \dot{z}_{sr} \end{bmatrix} = \mathbf{C}\mathbf{x} = \begin{bmatrix} 0 & 0 & 0 & 0 & 1 & -a & 0 & 0 \\ 0 & 0 & 0 & 0 & 1 & b & 0 & 0 \end{bmatrix} \mathbf{x} \tag{19}$$

$$\begin{cases} \mathbf{u}_{SOF}=\mathbf{K}_{SOF}\mathbf{y}=\begin{bmatrix} k_1 & k_2 \\ k_3 & k_4 \end{bmatrix}\mathbf{y} \\ \mathbf{u}_{SSOF1}=\mathbf{K}_{SSOF1}\mathbf{y}=\begin{bmatrix} k_1 & k_2 \\ k_2 & k_1 \end{bmatrix}\mathbf{y} \\ \mathbf{u}_{SSOF2}=\mathbf{K}_{SSOF2}\mathbf{y}=\begin{bmatrix} k_1 & 0 \\ 0 & k_2 \end{bmatrix}\mathbf{y} \end{cases} \tag{20}$$

In this paper, the controller gain matrices, $\mathbf{K}_{SOF}$, $\mathbf{K}_{SSOF1}$ and $\mathbf{K}_{SSOF2}$, that minimize J are called LQSOF, LQSSOF1 and LQSSOF2, respectively. It is known that, to date, there have been no analytic methods which find an optimal $\mathbf{K}_{SOF}$, $\mathbf{K}_{SSOF1}$ or $\mathbf{K}_{SSOF2}$ that minimizes J. To find the gain matrices that minimize J, the optimization problem is formulated as in (21), which has been known to be non-convex [9,12]. In Equation (21), $\mathbf{K}$ is either $\mathbf{K}_{SOF}$, $\mathbf{K}_{SSOF1}$ or $\mathbf{K}_{SSOF2}$, and $\mathbf{A}_c$ is the closed-loop (CL) system matrix, defined as $\mathbf{A} + \mathbf{B}_2\mathbf{K}\mathbf{C}$. As shown in (21), for a given $\mathbf{K}$, the stability of the CL system, $\mathbf{A}_c$, is checked and the Lyapunov equation is solved. To find the optimal solution of the problem in this paper, the heuristic optimization method, CMA-ES, is used as an optimizer [25,26].

$$\begin{aligned} \min_{\mathbf{K}} \quad & \text{trace}(\mathbf{S}) \\ s.t. \quad & \begin{cases} \mathbf{S} = \mathbf{S}^T > \mathbf{0} \\ \max(\text{Re}[\mathbf{A}_c]) < 0 \\ \mathbf{A}_c^T\mathbf{S} + \mathbf{S}\mathbf{A}_c + \mathbf{Q}+\mathbf{C}^T\mathbf{K}^T\mathbf{N}^T + \mathbf{N}\mathbf{K}\mathbf{C} + \mathbf{C}\mathbf{K}^T\mathbf{R}\mathbf{K}\mathbf{C} = \mathbf{0} \end{cases} \end{aligned} \tag{21}$$

3. Design of Adaptive Feedforward Algorithm

FxLMS has been applied to suspension control with active and semi-active suspensions [31–41]. In this paper, an FxLMS algorithm is adopted as an adaptive feedforward one to reduce the ω_y of the SPM [27,28]. Figure 6 shows the block diagram of the FxLMS algorithm. In Figure 6, $x(n)$, $e(n)$ and $u(n)$ are the reference, error and control signals, respectively. The control signal, $u(n)$, stands for the vertical force generated in the rear suspension.

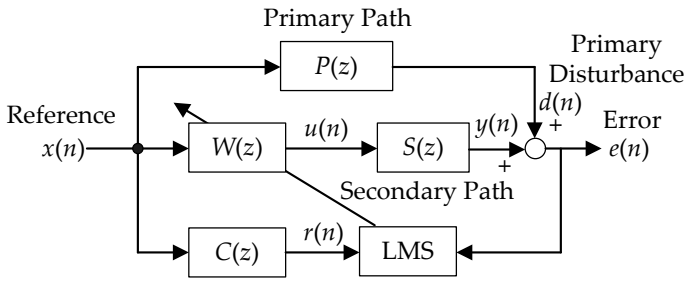


Figure 6. Block diagram of filtered-X LMS algorithm.

In this paper, the vertical acceleration at the SPMFC is selected as a reference signal because it can be easily measured by the accelerometer, acm_f, as in Figure 4. For motion sickness mitigation, the ω_y of the SPM is selected as an error, $e(n)$, as in Figure 6. As mentioned earlier, it is necessary to reduce the a_z and ω_y of the SPM over the frequency range of 0.8 to 8 Hz for motion sickness mitigation [10,11]. For this reason, the FxLMS algorithm is used to reduce ω_y while the LQ SOF controller tries to reduce a_z.

As shown in Figure 4, the control inputs, u_f and u_r, of LQ SOF controllers are applied to the front/rear suspensions, respectively. On the other hand, the control input of the FxLMS algorithm, $u(n)$, is applied to the rear suspension. Consequently, the control inputs of LQ SOF controllers and the FxLMS algorithm are summed and applied to the rear suspension.

The secondary path or control path, $S(z)$, is a signal flow from $u(n)$ to $e(n)$. For FxLMS, a secondary path is modeled by an FIR filter, and the filter is tuned by an LMS algorithm. Figure 7 shows the block diagram of the secondary path modeling procedure with the LMS algorithm. In Figure 7, $C(z)$ is the estimate of the secondary path. The coefficient of $C(z)$, i.e.,

$\mathbf{c}(n)$, is tuned by the LMS update rule, as given in Equation (22). In FxLMS, the coefficient of the filter $W(z)$, i.e., $\mathbf{w}(n)$, is updated with the LMS update rule, as given in Equation (23). In Equations (22) and (23), μ is the learning rate.

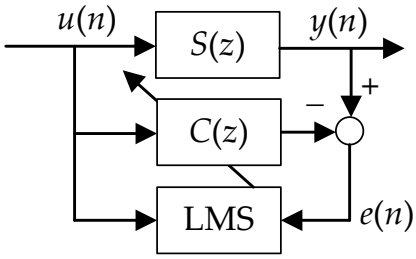


Figure 7. Block diagram of secondary path modeling with LMS algorithm.

The sampling rate and filter length of FxLMS should be set to cover the delay between the reference signal and the control one. For this reason, the product of the sampling rate and filter length should be larger than the delay between the reference and control signals.

$$\mathbf{c}(n+1) = \mathbf{c}(n) - \mu e(n)u(n) \tag{22}$$

$$\mathbf{w}(n+1) = \mathbf{w}(n) - \mu e(n)r(n) \tag{23}$$

A filtered-X recursive least squares (FxRLS) algorithm was adopted as an adaptive feedforward algorithm [46]. However, the control performance of FxRLS is nearly equivalent to that of FxLMS and the computational load of FxRLS is much larger than FxLMS. For this reason, FxRLS was not presented in this paper.

4. Simulation and Discussion

Simulation is undertaken to evaluate the performance of the LQ SOF controllers, LQSOF, LQSSOF1 and LSSSOF2, and the combined LQSOF1 and FxLMS. With simulation results, these controllers are compared to one another and it is observed which is effective for ride comfort enhancement and motion sickness mitigation.

4.1. Simulation Environment

The parameters of the half-car model, taken from the E-Class sedan provided in CarSim, can be found in previous work [9,12,47]. The MAVs in J are given in Table 1. For ride comfort enhancement and motion sickness mitigation, ξ_1, ξ_5 and ξ_7 were set low, as given in Table 1. In other words, these weights were set to reduce the a_z and ω_y of the SPM. In this paper, the actuator bandwidth is set to 5 Hz. Hereafter, a_z and ω_y are regarded as those of the SPM.

Table 1. MAVs in LQ cost function.

ξ_1	0.5 m/s^2	ξ_2	30.0 deg/s^2	ξ_3	10.0 deg/s
ξ_4	2.0 deg	ξ_5	0.1 m	ξ_6	0.1 m
ξ_7	10,000.0 N				

FxLMS was implemented with MATLAB/Simulink. In FxLMS, the FIR filters in Figure 5, $W(z)$ and $C(z)$, are implemented with a discrete-time transfer function in MATLAB/Simulink. The lengths of the FIR filter for the secondary path and FxLMS were set to 200. The sampling interval for FxLMS was set to 5 ms. As a result, the FxLMS can cover 1 sec, which is the delay between the reference signal and the control one. As given in previous research, the wheelbase of the vehicle is 3.05 m. Then, FxLMS can effectively work if the speed is faster than 11 km/h. The learning rate of FxLMS was set to 0.01. When modeling the secondary path from the rear active suspension to ω_y, the actuator dynamics with a bandwidth of 10 Hz were included.

When simulating LQ SOF controllers and the FxLMS algorithm on CarSim, large-sine-bump, sine-waved and bounce-sine-sweep roads were selected as road profiles. The large sine bump has a height and width of 0.1 m and 3.6 m, respectively. The sine-waved road has a wavelength and amplitude of 12.2 m and 0.05 m, respectively. The bounce-sine-sweep road, provided in CarSim, is shown in Figure 8; it is a sinusoidal bump with a decreasing wavelength and amplitude over time. The vehicle speeds were set to 10 m/s for the large sine bump and the bounce-sine-sweep road, and to 15 m/s for the sine-waved road.

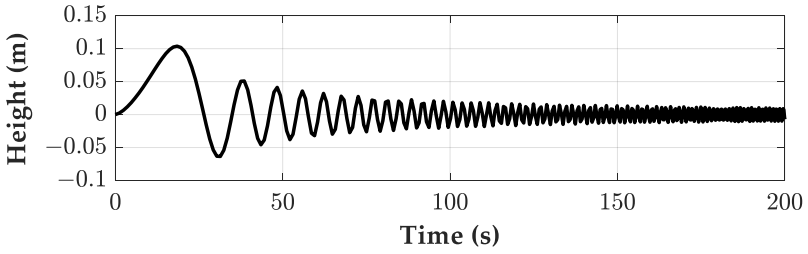


Figure 8. Bounce-sine-sweep road profile.

4.2. Frequency Response Analysis with the LQ SOF Controllers

With the weights given in Table 1, the gain matrices of LQSOF, LQSSOF1 and LQSSOF2, i.e., $\mathbf{K}_{SOF}$, $\mathbf{K}_{SSOF1}$ and $\mathbf{K}_{SSOF2}$, were calculated and given in Table 2. As shown in Table 2, the gain matrices of LQSOF and LQSSOF1 are nearly the same as each other. This is a natural result because the controller structures of LQSOF and LQSSOF1 are the same as each other and there is symmetry between the SPMFC and SPMRC along the pitch motion of the SPM. Consequently, LQSOF and LQSSOF1 are expected to show equivalent performance to each another. On the contrary, the gain matrix of LQSSOF2, $\mathbf{K}_{SSOF2}$, is different from those of LQSOF and LQSSOF1, as shown in Table 2. Because the off-diagonal elements in $\mathbf{K}_{SSOF2}$ are zero, LQSSOF2 is expected to show a relatively worse performance than LQSOF and LQSSOF1.

Table 2. The gain matrices of LQ SOF controllers calculated from the weights in Table 1.

LQSOF $\mathbf{K}_{SOF}$	$\begin{bmatrix} -17,521.0 & -5197.8 \\ -6272.8 & -17,057.0 \end{bmatrix}$	LQSSOF1 $\mathbf{K}_{SSOF1}$	$\begin{bmatrix} -17,123.0 & -5489.6 \\ -5489.6 & -17,123.0 \end{bmatrix}$
LQSSOF2 $\mathbf{K}_{SSOF2}$	$\begin{bmatrix} -14,334.0 & 0 \\ 0 & -13,960.0 \end{bmatrix}$		

Figure 9 shows the frequency response plots of LQR, LQSOF, LQSSOF1 and LQSSOF2 from z_{rf} to a_z and ω_y. These plots are obtained with the gain matrices in Table 2 and the SSE, (12). As shown in Figure 9, the controler performance is significantly improved by the LQR. It is natural that the performance of the LQR significantly outperforms LQSOF controllers because it uses all states for feedback. Compared to the LQR, LQSOF controllers are inferior because they use a smaller number of states than an LQR. The LQ SOF controllers show relatively good performance over the frequency range below 5 Hz because the actuator bandwidth is set to 5 Hz. In particular, LQSOF and LQSSOF1 are nearly identical to each other in terms of a_z and ω_y. This is caused by the fact that there is symmetry between the front and rear corners of the sprung mass along the vertical direction. This can be confirmed by the fact that the off-diagonal elements in $\mathbf{K}_{SOF}$ and $\mathbf{K}_{SSOF1}$ are nearly identical. On the contrary, LQSSFO2 shows relatively poor performance in terms of a_z. This is caused by the fact that the off-diagonal elements of $\mathbf{K}_{SSOF2}$ are zero. Moreover, this result means that the coupled effect between the vertical motions of the front/rear corners is negligible and that the vertical motions of the front/rear corners are independent of each other. From these results, it is shown that there are little differences among these LQ SOF controllers.

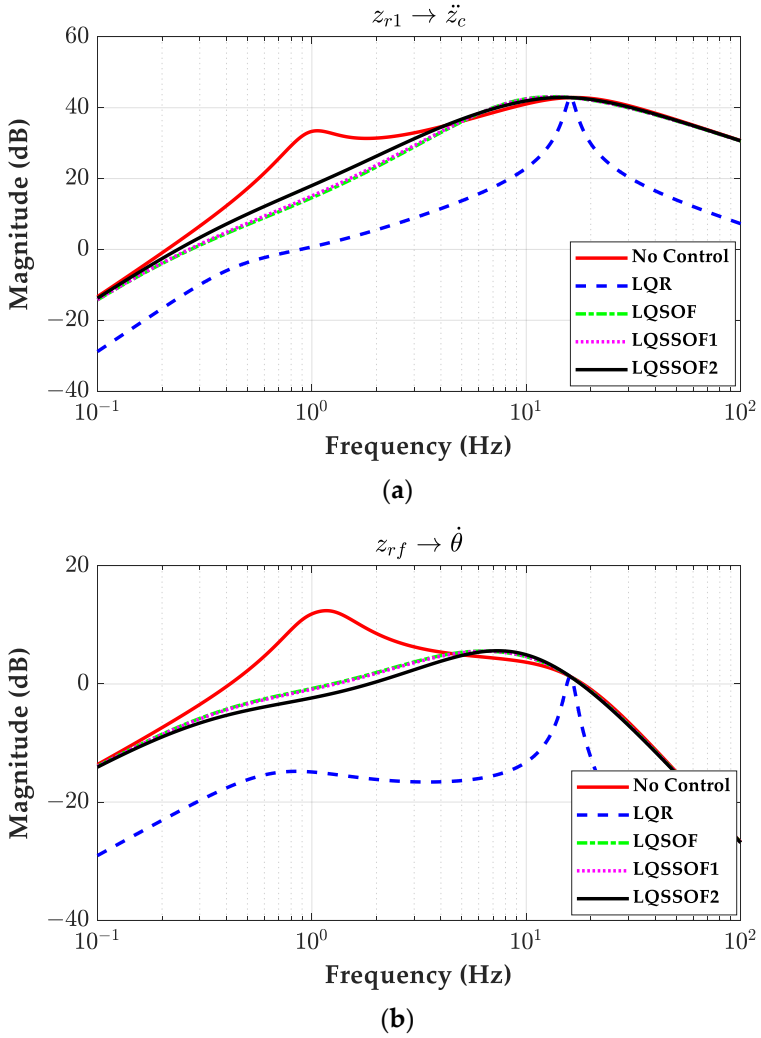


Figure 9. The frequency response plots of the SOF controllers. (**a**) Heave accelerations; (**b**) pitch rates.

4.3. Simulation with the LQ SOF Controllers on CarSim

Three LQ SOF controllers, LQSOF, LQSSOF1 and LQSSOF2, were simulated in a co-simulation environment with MATLAB/Simulink and CarSim. The large-sine-bump and sine-waved road were selected for simulation. The calculation procedure on vertical velocities at the front/rear corners given in Figure 5 was implemented in MATLAB/Simulink. When implementing it, a white noise was added into the sensor signals of the vertical accelerations measured at the front/rear corners.

Figures 10 and 11 show the simulation results of LQ SOF controllers on the large-sine-bump and the sine-waved road, respectively. Tables 3 and 4 show the maximum absolute values of the a_z and ω_y of the SPM over the simulation period on the large-sine-bump and sine-waved road, respectively. In Tables 3 and 4, the numbers in the parentheses stand for the percentage reduction to the uncontrolled case. The larger the numbers, the better the performance.

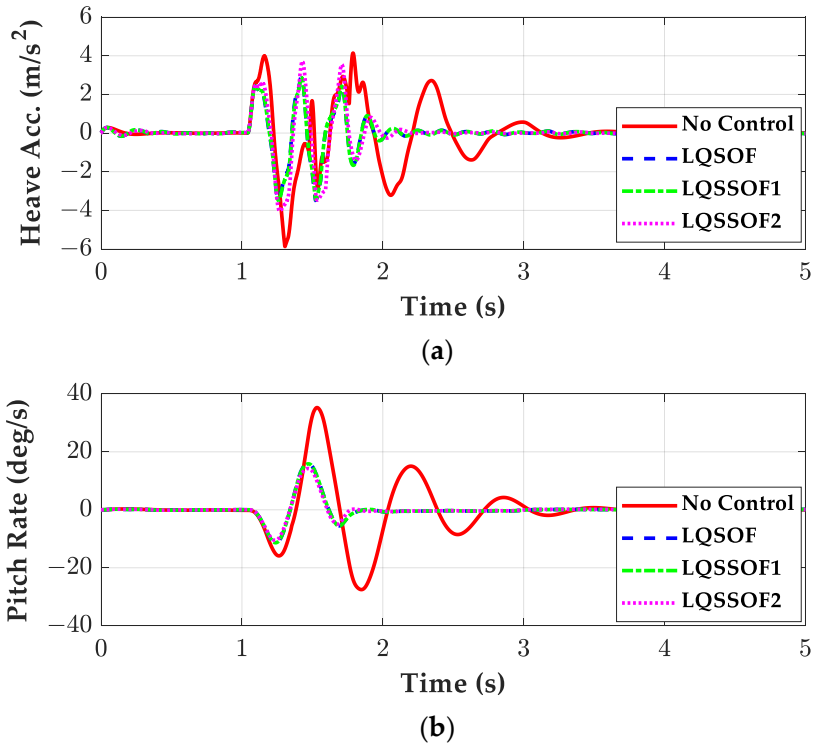


Figure 10. The simulation results of LQSOF, LQSSOF1 and LQSSOF2 for the large sine bump. (**a**) Heave accelerations; (**b**) pitch rates.

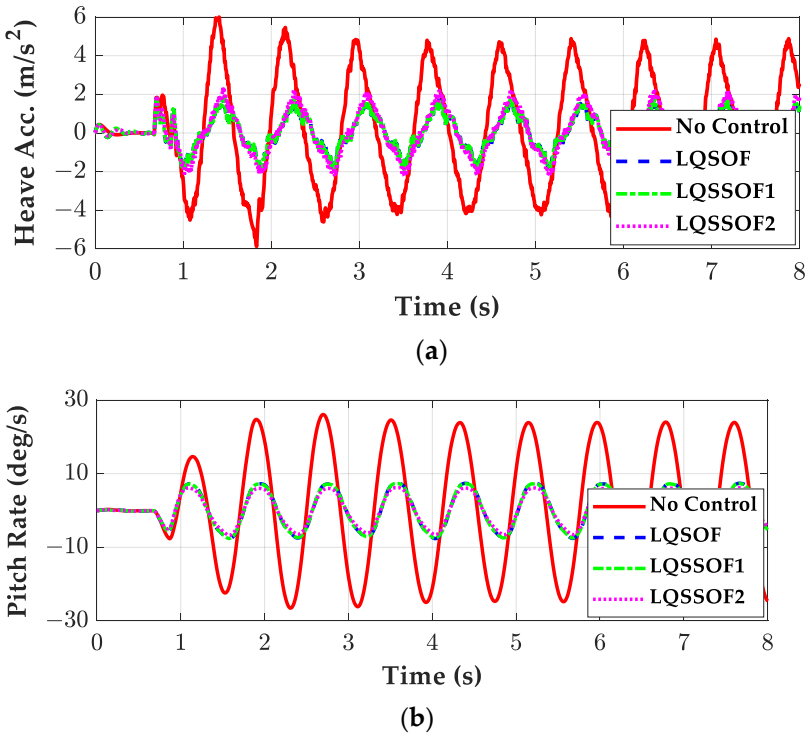


Figure 11. Simulation results of LQSOF, LQSSOF1 and LQSSOF2 on the sine-waved road. (**a**) Heave accelerations; (**b**) pitch rates.

Table 3. The maximum absolute a_z and ω_y calculated from the simulation results of LQ SOF controllers on the large sine bump.

Controller	Max $\lvert a_z \rvert$ (m/s^2)	Max $\lvert \omega_y \rvert$ (deg/s)
No Control	5.9	35.2
LQSOF	3.5 (41%)	16.0 (55%)
LQSSOF1	3.5 (41%)	15.8 (55%)
LQSSOF2	4.0 (32%)	14.2 (60%)

Table 4. The maximum absolute a_z and ω_y calculated from the simulation results of LQ SOF controllers on the sine-waved road.

Controller	Max $\lvert a_z \rvert$ (m/s^2)	Max $\lvert \omega_y \rvert$ (deg/s)
No Control	6.2	26.5
LQSOF	1.9 (69%)	7.7 (71%)
LQSSOF1	1.9 (69%)	7.6 (71%)
LQSSOF2	2.4 (61%)	6.7 (75%)

From the simulation results shown in Figures 10 and 11, it can be seen that three LQ SOF controllers give good performance in terms of ride comfort and motion sickness because a_z and ω_y were reduced by those SOF controllers. These results can be easily anticipated from the frequency response plots in Figure 9. Among them, LQSOF and LQSSOF1 show good performance in controlling a_z, compared to LQSSOF2, as can be seen in Table 3. Moreover, LQSOF and LQSOF1 show nearly identical performance to each other, as expected in Figure 9. On the other hand, LQSSOF2 shows slightly better performance than LQSOF and LQSSOF1 in terms of the pitch rate, in spite of the deterioration of a_z.

If ξ_1 is set to a lower value than 0.5 m/s^2, as given in Table 1, better performance can be obtained for those SOF controllers in terms of a_z. However, a_z cannot converge to zero. In other words, the smaller ξ_1 is, the larger the oscillation of a_z is. This is caused by the excessive damping of the controller, which has a negative effect on ride comfort. For this reason, one should pay attention to not make ξ_1 too small.

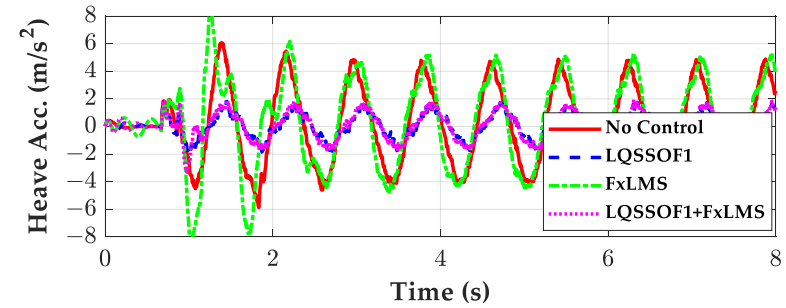
As can be seen in Tables 3 and 4, LQSSOF1 is the simplest one among the LQ SOF controllers and gives relatively better results. For this reason, LQSSOF1 is used as an LQ SOF controller hereafter.

4.4. Simulation with FxLMS and LQ SOF Controllers on CarSim

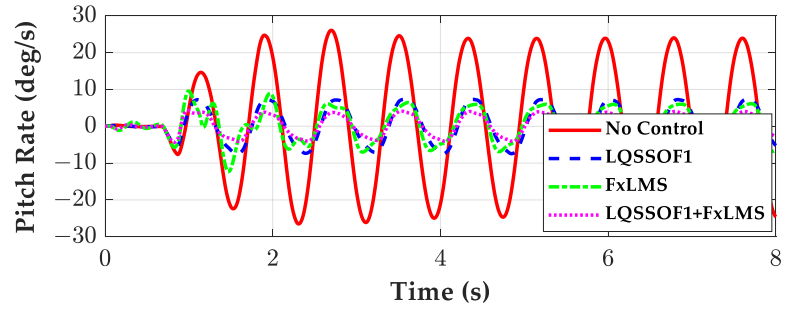
For simulation, the LQ SOF controller, i.e., LQSSOF1, is combined with FxLMS in this subsection. Regarding the usage of these two controllers, four cases, i.e., no control, FxLMS, LQSSOF1 and LQSSOF1 + FxLMS, are compared in this subsection. For road profiles, the sine-waved and bounce-sine-sweep roads were selected.

Figure 12 shows the simulation results of four cases on the sine-waved road. Table 5 shows the maximum absolute values of a_z and ω_y over the simulation period from 1 s to 8 s on the sine waved road. In Table 5, the numbers in the parentheses stand for the percentage reduction to the uncontrolled case. The negative sign means that the percentage increases.

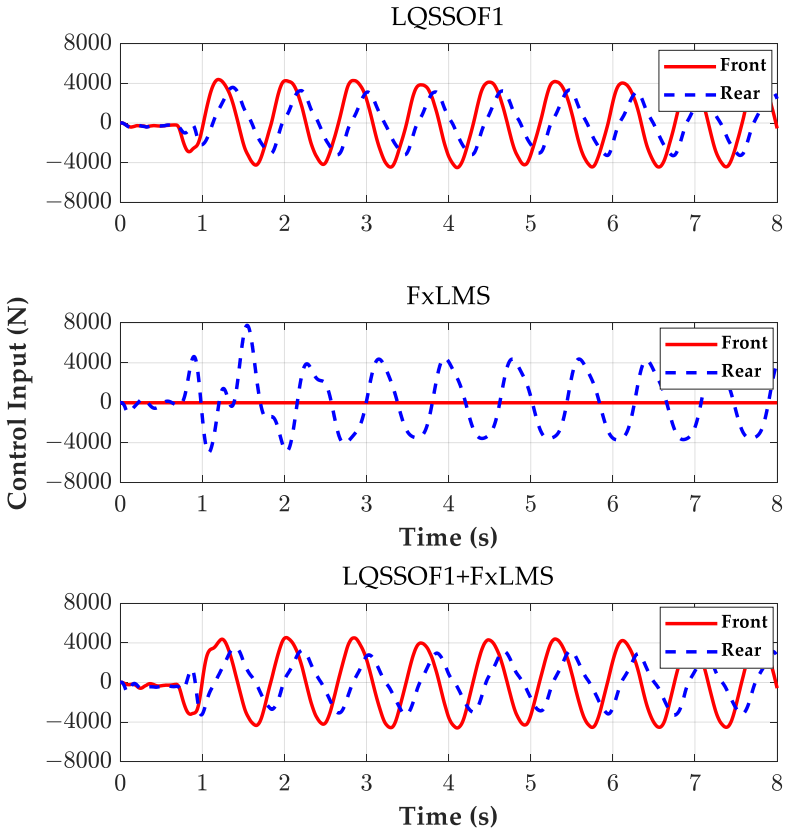
As shown in Figure 12, LQSSOF1 and LQSSOF1 + FxLMS can effectively reduce a_z and ω_y. From the simulation results given in Figure 12 and Table 5, it can be seen that FxLMS cannot reduce a_z while LQSSOF1 reduces it, and that FxLMS can only reduce ω_y. This is a natural consequence, because the secondary path in FxLMS was modeled with ω_y. Combined with LQSSOF1, FxLMS can reduce ω_y further from 54% to 84%, as given in Table 5. However, a_z is reduced slightly from 68% to 58% by FxLMS, as shown in Table 5. This is caused by the fact that the control input of FxLMS is applied only to the rear suspension. In other words, FxLMS slightly destroyed the symmetry between the front/rear corners of the LQ SOF controller.



(**a**)



(**b**)



(**c**)

Figure 12. The simulation results of no control, LQSSOF1, FxLMS and LQSSOF1 + FxLMS on the sine-waved road. (**a**) Heave accelerations; (**b**) pitch rates; (**c**) control inputs.

Table 5. The maximum absolute a_z and ω_y calculated from the simulation results of LQSOF1 and FxLMS on the sine-waved road.

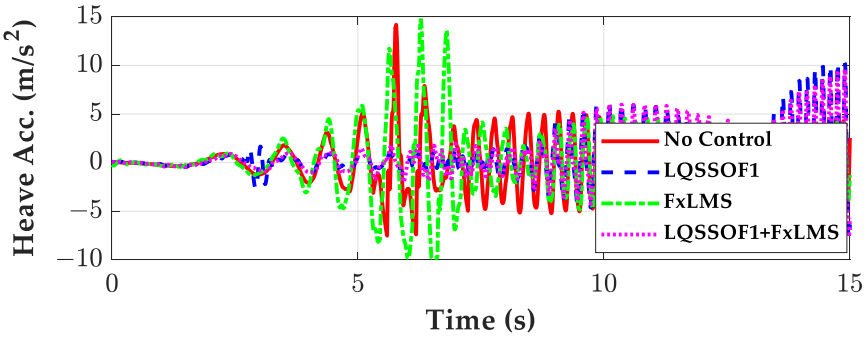
Controller	Max $\lvert a_z \rvert$ (m/s^2)	Max $\lvert \omega_y \rvert$ (deg/s)
No Control	6.2	26.5
LQSSOF1	2.0 (68%)	7.6 (71%)
FxLMS	8.6 (−39%)	12.3 (54%)
LQSSOF1 + FxLMS	2.6 (58%)	4.3 (84%)

From this feature of FxLMS, a simpler control structure can be derived such that the front active suspension is controlled by an LQ SOF controller designed with a quarter-car model and the rear active suspension is controlled by FxLMS.

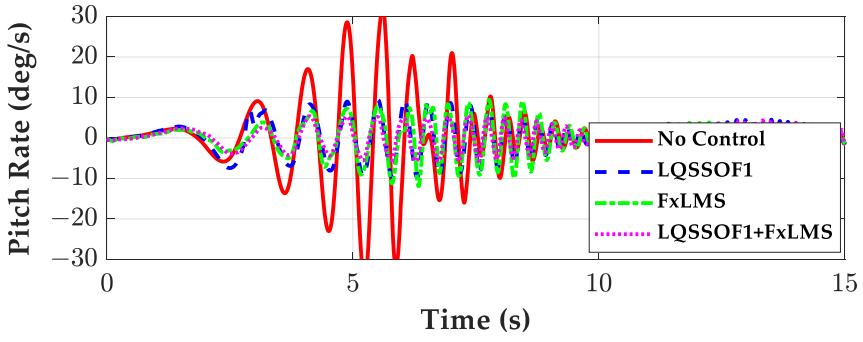
Figure 13 shows the simulation results of four cases on the bounce-sine-sweep road. Table 6 shows the maximum absolute values of a_z and ω_y over the simulation period from 1 s to 8 s on the bounce-sine-sweep road. Figure 14 shows the frequency response plots of four cases obtained from the simulation results.

Table 6. The maximum absolute a_z and ω_y calculated from the simulation results of LQSOF1 and FxLMS on the bounce-sine-sweep road.

Controller	Max $\lvert a_z \rvert$ (m/s^2)	Max $\lvert \omega_y \rvert$ (deg/s)
No Control	14.2	34.8
LQSSOF1	2.6 (82%)	9.7 (72%)
FxLMS	14.8 (−4%)	11.9 (66%)
LQSSOF1 + FxLMS	2.0 (86%)	5.8 (83%)

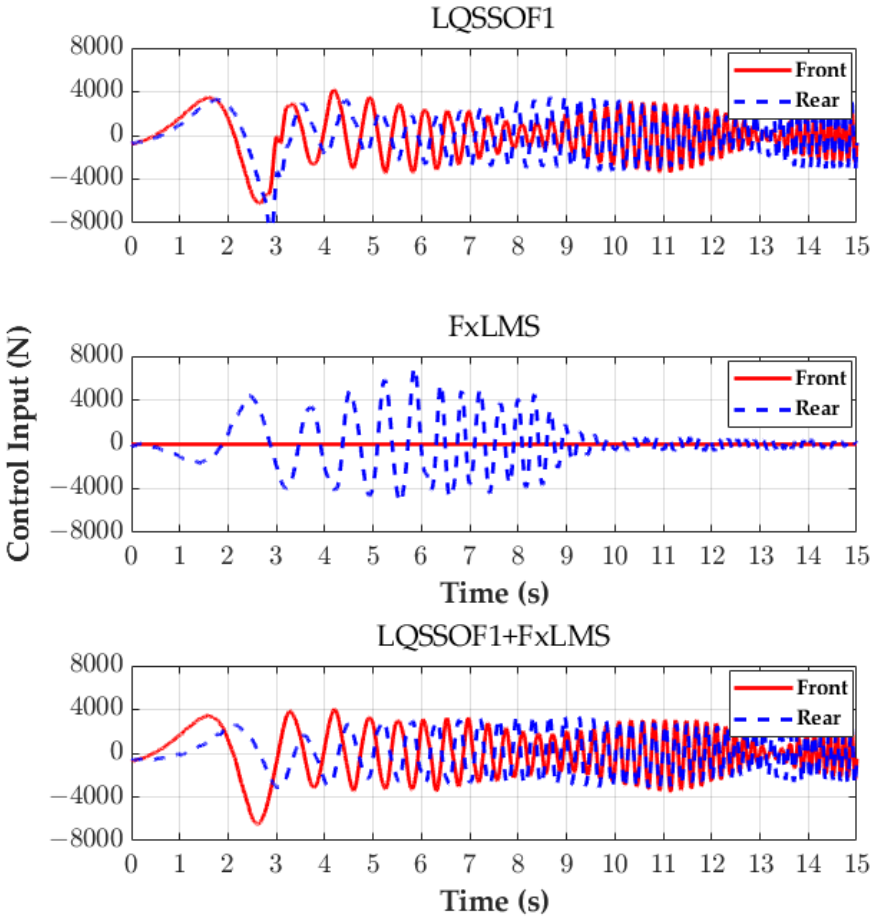


(**a**)



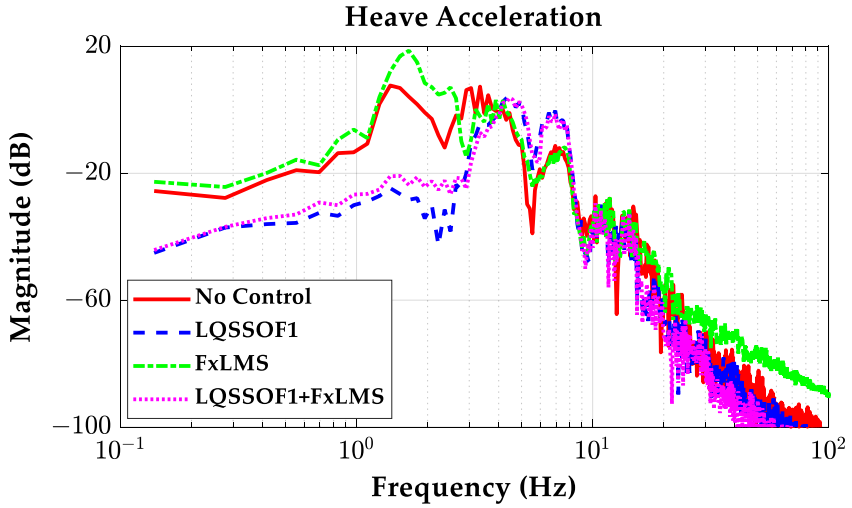
(**b**)

Figure 13. *Cont.*



(**c**)

Figure 13. The simulation results of no control, LQSSOF1, FxLMS and LQSSOF1 + FxLMS on the bounce-sine-sweep road. (**a**) Heave accelerations; (**b**) pitch rates; (**c**) control inputs.



(**a**)

Figure 14. *Cont.*

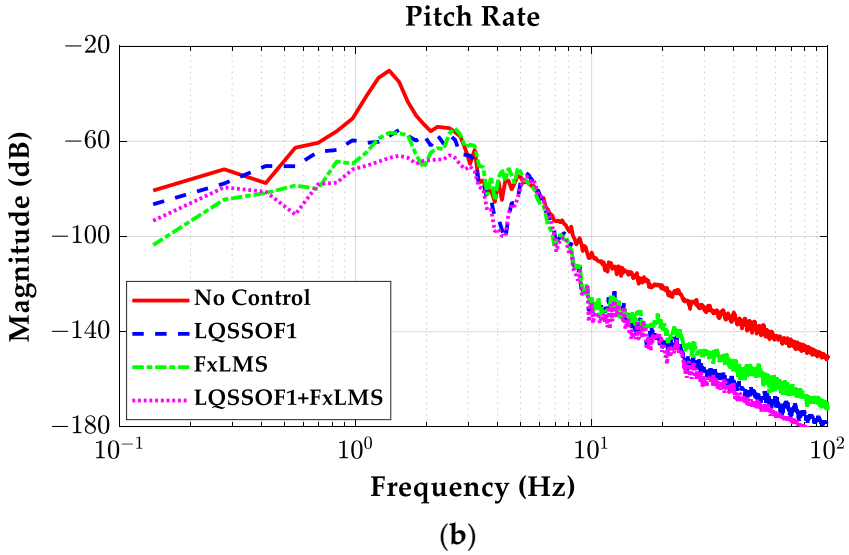


Figure 14. The frequency response plots of no control, LQSSOF3, FxLMS and LQSSOF3 + FxLMS on the bounce-sine-sweep road. (**a**) Heave accelerations; (**b**) pitch rates.

As shown in Figure 13 and Table 6, the simulation results on the bounce-sine-sweep road show the same tendency as those on the sine-waved road. Figure 13 demonstrates the fact that LQSSOF1 and LQSSOF1 + FxLMS can significantly reduce a_z and ω_y below 4 Hz, which is expected from Figure 8. Over the frequency range below 4 Hz, the front/rear control inputs have opposite phases, as shown in Figure 13c. From the simulation results given in Figure 13 and Table 6, it can be concluded that FxLMS can reduce ω_y further than LQSSOF1, from 72% to 83%. Instead, a_z was slightly reduced near 2 Hz by FxLMS, as shown in Figure 14a. This result means that FxLMS slightly destroyed the symmetry between the front and rear corners of the LQ SOF controller near 2 Hz.

5. Conclusions

In this paper, LQ SOF controllers and a filtered-X LMS algorithm were designed and applied to reduce the heave acceleration and the pitch rate of the sprung mass for ride comfort enhancement and motion sickness mitigation. To avoid a full-state feedback, which is hard to implement in a real vehicle, the structured SOF structure was selected and optimized with an LQ cost function. FxLMS was applied with vertical acceleration on the front suspension as a reference signal and the pitch rate as an error. To validate the proposed method in terms of ride comfort and motion sickness, simulation was conducted on CarSim. From the simulation results, it was shown that the proposed method is quite effective in terms of enhancing ride comfort and mitigating motion sickness. It was also shown that FxLMS can reduce only the pitch rate of the SPM, and that FxLMS can reduce the pitch rate of the SPM further if combined with the LQ SOF controllers. In future work, the proposed method will be validated by an experiment on small-scale devices.

Author Contributions: Conceptualization, S.Y.; methodology, S.Y.; software, J.K. and S.Y.; validation, J.K. and S.Y.; formal analysis, S.Y.; investigation, J.K. and S.Y.; resources, S.Y.; data curation, J.K. and S.Y.; writing—original draft preparation, J.K. and S.Y.; writing—review and editing, J.K.; visualization, J.K.; supervision, S.Y.; funding acquisition, S.Y. All authors have read and agreed to the published version of the manuscript.

Funding: This research received no external funding.

Data Availability Statement: The original contributions presented in the study are included in the article; further inquiries can be directed to the corresponding author/s.

Acknowledgments: This study was supported by the Research Program funded by Seoul National University of Science and Technology.

Conflicts of Interest: The authors declare no conflicts of interest.

Nomenclature

LQR	Linear quadratic regulator
LQSOF	Linear quadratic static output feedback
LQSSOF	Linear quadratic structured static output feedback
SOF	Static output feedback
SPM	Sprung mass or vehicle body
SPMFC	Front corner of sprung mass
SPMRC	Rear corner of sprung mass
SSE	State-space equation
SSOF	Structured static output feedback
WBPCS	Wheelbase preview control scheme
a, b	Distances from center of gravity of sprung mass to front/rear corners (m)
$a_z = \ddot{z}_c$	Vertical or heave acceleration of sprung mass (m/s^2)
b_{sf}, b_{sr}	Damping coefficient of damper at front/rear suspensions (N·s/m)
I_y	Pitch moment of inertia (kg·m^2)
J	LQ cost function used for LQR, LQSOF and LQSSOF
k_{sf}, k_{sr}	Stiffness of spring at front/rear suspensions (N/m)
k_{tf}, k_{tr}	Stiffness of front/rear tires (N/m)
m_s	Sprung mass (kg)
m_{uf}, m_{ur}	Unsprung mass under front/rear suspensions (kg)
u_f, u_r	Forces generated by actuator at front/rear suspensions (N)
z_c	Heave displacement at center of gravity of sprung mass (m)
z_{rf}, z_{rr}	Road elevation acting on front/rear tires (m)
z_{sf}, z_{sr}	Vertical displacement of front/rear corners of sprung mass (m)
z_{uf}, z_{ur}	Vertical displacement of front/rear wheel centers (m)
ξ_i	Maximum allowable value (MAV) of weight in LQ cost function
$\omega_y = \dot{\theta}$	Pitch rate of sprung mass (rad/s)
ρ_i	Weight in LQ cost function
θ	Pitch angle of sprung mass (rad)

References

1. Khan, M.A.; Sayed, H.E.; Malik, S.; Zia, T.; Khan, J.; Alkaabi, N.; Ignatious, H. Level-5 autonomous driving—Are we there yet? a review of research literature. *ACM Comput. Surv.* **2022**, *55*, 1–38. [CrossRef]
2. Omeiza, D.; Webb, H.; Jirotka, M.; Kunze, L. Explanations in autonomous driving: A survey. *IEEE Trans. Intell. Trans. Sys.* **2022**, *23*, 10142–10162. [CrossRef]
3. Zhao, J.; Zhao, W.; Deng, B.; Wang, Z.; Zhang, F.; Zheng, W.; Cao, W.; Nan, J.; Lian, Y.; Burke, A.F. Autonomous driving system: A comprehensive survey. *Expert Syst. Appl.* **2024**, *242*, 122836. [CrossRef]
4. Diels, C.; Bos, J.E. Self-driving carsickness. *Appl. Ergon.* **2016**, *53*, 374–382. [CrossRef] [PubMed]
5. Asua, E.; Gutiérrez-Zaballa, J.; Mata-Carballeira, O.; Ruiz, J.A.; del Campo, I. Analysis of the motion sickness and the lack of comfort in car passengers. *Appl. Sci.* **2022**, *12*, 3717. [CrossRef]
6. Xie, W.; He, D.; Wu, G. Inducers of motion sickness in vehicles: A systematic review of experimental evidence and meta-analysis. *Transp. Res. Part F Traffic Psychol. Behav.* **2023**, *99*, 167–188. [CrossRef]
7. *ISO 2631-1*; Mechanical Vibration and Shock—Evaluation of Human Exposure to Whole-Body Vibration—Part 1: General Requirements. International Organization for Standardization: Geneva, Switzerland, 1997.
8. Rimell, A.N.; Mansfield, N.J. Design of digital filters for frequency weightings required for risk assessments of workers exposed to vibration. *Ind. Health* **2007**, *45*, 512–519. [CrossRef]
9. Kim, J.; Yim, S. Design of static output feedback suspension controllers for ride comfort improvement and motion sickness reduction. *Processes* **2024**, *12*, 968. [CrossRef]
10. Ekchian, J.; Graves, W.; Anderson, Z.; Giovanardi, M.; Godwin, O.; Kaplan, J.; Ventura, J.; Lackner, J.R.; DiZio, P. *A High-Bandwidth Active Suspension for Motion Sickness Mitigation in Autonomous Vehicles*; SAE Technical Paper 2016-01-1555; SAE International: Warrendale, PA, USA, 2016.

11. DiZio, P.; Ekchian, J.; Kaplan, J.; Ventura, J.; Graves, W.; Giovanardi, M.; Anderson, Z.; Lackner, J.R. An active suspension system for mitigating motion sickness and enabling reading in a car. *Aerosp. Med. Hum. Perform.* **2018**, *89*, 822–829. [CrossRef]
12. Jeong, Y.; Yim, S. Design of active suspension controller for ride comfort enhancement and motion sickness mitigation. *Machines* **2024**, *12*, 254. [CrossRef]
13. Poussot-Vassal, C.; Spelta, C.; Sename, O.; Savaresi, S.M.; Dugard, L. Survey and performance evaluation on some automotive semi-active suspension control methods: A comparative study on a single-corner model. *Annu. Rev. Control* **2012**, *36*, 148–160. [CrossRef]
14. Tseng, H.E.; Hrovat, D. State of the art survey: Active and semi-active suspension control. *Veh. Syst. Dyn.* **2015**, *53*, 1034–1062. [CrossRef]
15. Cao, D.; Song, X.; Ahmadian, M. Editors' perspectives: Road vehicle suspension design, dynamics, and control. *Veh. Syst. Dyn.* **2011**, *49*, 3–28. [CrossRef]
16. Wilson, D.A.; Sharp, R.S.; Hassan, S.A. The application of linear optimal control theory to the design of active automobile suspensions. *Veh. Syst. Dyn.* **1987**, *15*, 105–118. [CrossRef]
17. Hac, A. Optimal linear preview control of active vehicle suspension. *Veh. Syst. Dyn.* **1992**, *21*, 167–195. [CrossRef]
18. Abdel-Hady, M.B.A.; Crolla, D.A. Active suspension control algorithms for a four wheel vehicle model. *Int. J. Veh. Des.* **1992**, *13*, 144–158.
19. Mudduluru, S.R.; Chizari, M. Quarter and Full Car Models Optimisation of Passive and Active Suspension System Using Genetic Algorithm. *arXiv* **2021**, arXiv:2101.12629.
20. Theunissen, J.; Tota, A.; Gruber, P.; Dhaens, M.; Sorniotti, A. Preview-based techniques for vehicle suspension control: A state-of-the-art review. *Annu. Rev. Control* **2021**, *51*, 206–235. [CrossRef]
21. Camino, J.F.; Zampieri, D.E.; Peres, P.L.D. Design of a vehicular suspension controller by static output feedback. In Proceedings of the American Control Conference, San Diego, CA, USA, 2–4 June 1999; pp. 3168–3171.
22. Elmadany, M.M.; Al-Majed, M.I. Quadratic synthesis of active controls for a quarter-car model. *J. Vib. Control* **2001**, *7*, 1237–1252. [CrossRef]
23. Park, M.; Yim, S. Design of static output feedback and structured controllers for active suspension with quarter-car model. *Energies* **2021**, *14*, 8231. [CrossRef]
24. Jeong, Y.; Shon, Y.; Chang, S.; Yim, S. Design of static output feedback controllers for an active suspension system. *IEEE Access* **2022**, *10*, 26948–26964. [CrossRef]
25. Hansen, N.; Muller, S.D.; Koumoutsakos, P. Reducing the time complexity of the derandomized evolution strategy with covariance matrix adaptation (CMA-ES). *Evol. Comput.* **2003**, *11*, 1–18. [CrossRef] [PubMed]
26. Hansen, N. The CMA evolution strategy: A comparing review. In *Towards a New Evolutionary Computation. Advances in Estimation of Distribution Algorithms*; Lozano, J.A., Larrañga, P., Inza, I., Bengoetxea, E., Eds.; Springer: Berlin/Heidelberg, Germany, 2006; pp. 75–102.
27. Widrow, B.; Stearns, S.D. *Adaptive Signal Processing*; Prentice Hall, International (UK) Limited: London, UK, 1985.
28. Kuo, S.M.; Morgan, D.R. *Active Noise Control Systems-Algorithms and DSP Implementations*; Wiley: New York, NY, USA, 1996.
29. Lu, L.; Yin, K.; de Lamare, R.C.; Zheng, Z.; Yu, Y.; Yang, X.; Chen, B. A survey on active noise control in the past decade—Part I: Linear systems. *Signal Process.* **2021**, *183*, 108039. [CrossRef]
30. Lu, L.; Yin, K.; de Lamare, R.C.; Zheng, Z.; Yu, Y.; Yang, X.; Chen, B. A survey on active noise control in the past decade–Part II: Nonlinear systems. *Signal Process.* **2021**, *181*, 107929. [CrossRef]
31. Kwak, B.H.; Kim, H.S.; Park, Y. Adaptive control of active suspension systems with preview. In Proceedings of the 13th Korean Automatic Control Conference (KACC), Busan, Republic of Korea, 15–17 October 1998. (In Korean).
32. Feng, J.; Bei, S.; Yuan, C.; Zhang, L. Research on wheelbase preview control for vehicle semi-active suspension based on neural networks, 2009. In Proceedings of the Third International Symposium on Intelligent Information Technology Application, Nanchang, China, 21–22 November 2009.
33. Krauze, P.; Kasprzyk, J. FxLMS algorithm with preview for vibration control of a half-car model with magnetorheological dampers. In Proceedings of the 2014 IEEE/ASME International Conference on Advanced Intelligent Mechatronics (AIM), Besançon, France, 8–11 July 2014.
34. Strohm, J.N.; Lohmann, B. A fast convergence FxLMS algorithm for vibration damping of a quarter car. In Proceedings of the 2018 IEEE Conference on Decision and Control (CDC), Miami, FL, USA, 17–19 December 2018.
35. Krauze, P.; Kasprzyk, J. FxLMS control of an off-road vehicle model with magnetorheological dampers. In *Advanced, Contemporary Control. Advances in Intelligent Systems and Computing*; Bartoszewicz, A., Kabziński, J., Kacprzyk, J., Eds.; Springer: Cham, Switzerland, 2020; Volume 1196.
36. An, K.; Kim, D.; Kim, S.; Choi, J.; Lee, S.K.; Im, M.; Cho, H.S.; An, C. Active vibration control system for attenuation of structure borne road noise by tire cavity resonance using piezoelectric stack actuators. *SAE Tech. Pap.* **2024**. [CrossRef]
37. Okda, S.; Nampally, S.R.; Fontana, M.; Herold, S.; Nordmann, R.; Rinderknecht, S.; Melz, T. Active vibration control of gearbox housing using inertial mass actuators. *Smart Mater. Struct.* **2024**, *33*, 095008. [CrossRef]
38. Jiang, J.; Gao, Z.; Zhang, H.; Zhu, X. Research on active vibration control of blade using variable-step-size filtered-x least mean square algorithm. *J. Vib. Control* 2024, Online First. [CrossRef]

39. Wu, T.; Chen, T.; Yan, H.; Qu, J. An Improved FXLMS algorithm based on error weight for active vibration control of plates. *J. Vib. Eng. Technol.* **2024**, *12*, 3289–3303. [CrossRef]
40. Chai, K.; Liu, Y.S.; Hu, B.J. Multi-channel decentralized decoupling FxLMS algorithm and active vibration control experiment. *J. Low Freq. Noise Vib. Act. Control* **2024**. Online First. [CrossRef]
41. Liu, T.; Liu, C.; Zhang, Z. Adaptive active vibration control for composite laminated plate: Theory and experiments. *Mech. Syst. Signal Process.* **2024**, *206*, 110876. [CrossRef]
42. Bryson, A.E., Jr.; Ho, Y. *Applied Optimal Control*; Hemisphere: New York, NY, USA, 1975.
43. Hong, K.; Sohn, H.; Hedrick, J.K. Modified skyhook control of semi-active suspensions: A new model, gain scheduling, and hardware-in-the-loop tuning. *J. Dyn. Syst. Meas. Control* **2002**, *124*, 158–167. [CrossRef]
44. Ding, R.; Wang, R.; Meng, X.; Chen, L. Energy consumption sensitivity analysis and energy-reduction control of hybrid electromagnetic active suspension. *Mech. Syst. Signal Process.* **2019**, *134*, 106301. [CrossRef]
45. Liu, W.; Wang, R.; Ding, R.; Meng, X.; Yang, L. On-line estimation of road profile in semi-active suspension based on unsprung mass acceleration. *Mech. Syst. Signal Process.* **2020**, *135*, 106370. [CrossRef]
46. Akhtar, M.T. Developing a new filtered-X recursive least squares adaptive algorithm based on a robust objective function for impulsive active noise control systems. *Appl. Sci.* **2023**, *13*, 2715. [CrossRef]
47. Mechanical Simulation Corporation. *CarSim Data Manual*; Version 8; Mechanical Simulation Corporation: Ann Arbor, MI, USA, 2009.

Disclaimer/Publisher's Note: The statements, opinions and data contained in all publications are solely those of the individual author(s) and contributor(s) and not of MDPI and/or the editor(s). MDPI and/or the editor(s) disclaim responsibility for any injury to people or property resulting from any ideas, methods, instructions or products referred to in the content.